ACS APPLIED MATERIALS & INTERFACES
Research Article
www.acsami.org

Ethyl Cellulose and Cetrimonium Bromide Assisted Synthesis of Mesoporous, Hexagon Shaped ZnO Nanodisks with Exposed ±{0001} Polar Facets for Enhanced Photovoltaic Performance in Quantum Dot Sensitized Solar Cells

Tridip Ranjan Chetia, Mohammad Shaad Ansari, and Mohammad Qureshi*

Materials Science Laboratory, Department of Chemistry, Indian Institute of Technology Guwahati, Guwahati 781039, Assam, India

S *Supporting Information*

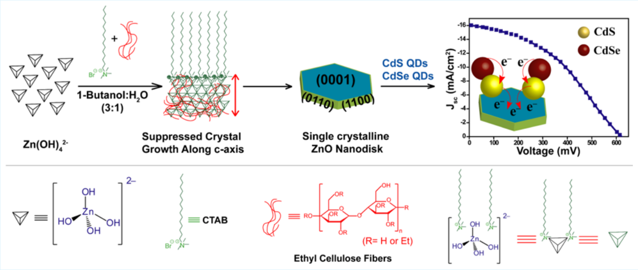

ABSTRACT: Hexagon shaped mesoporous zinc oxide nanodisks (ZnO NDs) with exposed ±{0001} polar facets have been synthesized by using ethyl cellulose (EC) and cetrimonium bromide (CTAB) as the capping and structure directing agents. We have characterized ZnO NDs using analytical techniques, such as powder X-ray diffraction (PXRD), diffuse reflectance UV−visible (UV−vis) spectroscopy, photoluminescence (PL) spectroscopy, field emission scanning electron microscopy (FESEM), transmission electron microscopy (TEM), and Brunauer−Emmett−Teller (BET) surface area analysis and proposed a plausible mechanism for the formation of ZnO NDs. EC molecules form a colloidal solution in a 1-butanol:water (3:1) solvent system having a negative zeta potential ($\zeta \approx -32$ mV) value which can inhibit CTAB assisted *c*-axis growth of ZnO crystal and encourage the formation of ZnO NDs. In the control reactions carried out in presence of only CTAB and only EC, formation of hexagonal ZnO nanorods (NRs) and ZnO nanosheets (NSs) composed of numerous ZnO nanoparticles are observed, respectively. Photovoltaic properties of ZnO NDs as compared to ZnO NRs, ZnO NSs, and conventional ZnO nanoparticles (NPs) are investigated by co-sensitizing with CdS/CdSe quantum dots (QDs). An ∼35% increase in power conversion efficiency (PCE, η) is observed in ZnO NDs ($\eta \approx 4.86\%$) as compared to ZnO NPs ($\eta \approx 3.14\%$) while the values of PCE for ZnO NR and ZnO NS based devices are found to be ∼2.52% and ∼1.64%, respectively. Enhanced photovoltaic performance of the ZnO NDs based solar cell is attributed to an efficient charge separation and collection, boosted by the exposed ±(0001) facets apart from the single crystalline nature, better light-scattering effects, and high BET surface area for sensitizer particle adsorption. Electrochemical impedance spectroscopy (EIS) analysis further reveals that the charge recombination resistance and photoinduced electron lifetime are substantially higher in the ZnO ND based device than in ZnO NR, ZnO NP, and ZnO NS based devices, which demonstrates a slower electron−hole (e^-−h^+) recombination rate and faster charge migration through the single crystalline ZnO NDs.

KEYWORDS: *crystal facets, metal oxide, co-sensitization, photoanode, charge separation, redox couple*

1. INTRODUCTION

Zinc oxide (ZnO) is a virtuous candidate for utilization as a photoanodic material in the semiconductor quantum dot sensitized solar cells (QSSC) accredited to its numerous intrinsic characteristics such as a stable wurtzite crystal structure with a wide band gap (∼3.37 eV), high carrier mobility (∼115−155 $cm^2 V^{-1} s^{-1}$), and large exciton binding energy (∼60 meV).[1,2] ZnO can be tailored into various architectures such as zero- (0-D), one- (1-D), and two-dimensional (2-D) nanostructures as well as three-dimensional (3-D) microstructures due to its ease of crystallization and anisotropic growth behavior, which allow one to control the electrical transport and optical (sensitizer particle loading and light-scattering) properties of the photoanodes for an enhanced solar cell performance.[3−5] The 0-D and 3-D structures of ZnO provide a larger surface area for sensitizer adsorption, while 1-D and 2-D nanostructures offer direct and faster transport pathways for photogenerated electrons.[6] For example Liu et al. have presented a greener way to grow vertically aligned 1-D ZnO nanorods which has great potential for photovoltaic application.[7] However, insufficient internal active surface area of vertically grown 1-D ZnO nanostructures always limit their energy conversion performance. The limiting factor of 0-D and 3-D structures is the charge collection, wherein the photogenerated electrons undertake a random movement through the film and interact repeatedly with the trap sites in grain boundaries.[8] Although a number of size- and shape-dependent morphologies of ZnO, such as nanoparticles,[9,10] nanowires,[11−14] nanotubes,[15] hierarchical tetrapod-like structures,[16] nanosheets,[17] nanoflowers,[18] microspheres,[19] and hollow microspheres,[6,20] etc., are explored

Received: February 3, 2015
Accepted: May 13, 2015
Published: May 13, 2015

DOI: 10.1021/acsami.5b01039
ACS Appl. Mater. Interfaces 2015, 7, 13266−13279

as candidates for photoanodic material to fabricate efficient QSSCs as well as dye sensitized solar cells (DSSCs), there are fewer reports about the possibility of exploring the exposed facets in enhancing the efficiency of the devices[21,22] as compared to the photocatalytic activity.[23−27] In most of the synthetic methods, 1-D hexagonal ZnO nanowires or nanorods with exposed nonpolar $\pm(10\bar{1}0)$, $\pm(1\bar{1}00)$, and $\pm(01\bar{1}0)$ facets are generally produced due to their intrinsic high energy of the $\pm(0001)$ polar surfaces and faster growth along the [0001] direction.[28] In order to tailor the exposure of ZnO crystal facets, it is necessary to minimize the surface energy of the polar high energy crystal facets during crystal growth. Selective adsorption of appropriate capping agents or additives on these polar facets can compensate the surface charges and alter the crystal growth habits of ZnO. Capping agents, such as oleic acid,[29] citrate ions,[30] sodium bis(2-ethylhexyl) sulfosuccinate or AOT,[31] starch,[32] polyvinylpyrrolidone,[33] poly(ethylene glycol),[34] pectin,[35] and gelatin,[36] etc., are utilized in the synthesis processes of ZnO to control growth kinetics of high energy facets and to obtain the anticipated size and shape. There are a few reports on the synthesis of hexagonal ZnO nanodisks by wet chemical route, however, rarely studied for the quantum dot (QD) loading so far,[37,38] although they have got great potential as a photoanodic material for efficient QSSCs. QDs have several advantages over the organic dye molecules such as higher stability and higher extinction coefficient,[39] tunable absorption edge controlled by the particle size,[40,41] generation of multiple electron−hole pairs per photon,[42] and low cost. Due to these distinctive features of semiconductor QDs as light harvesters, QSSCs are gaining considerable attention as a next generation photovoltaics.[43,44] Among various QDs that are used in QSSCs, for example, CdS,[45,46] CdSe,[47] PbS,[48] $CuInS_2$,[49] Sb_2S_3,[50] and InP,[51] etc., co-sensitization of metal oxide by CdS/CdSe is attractive owing to their high potential of light absorption in the visible light region, efficient transfer of photogenerated charge carrier, and ease of deposition techniques.[52,53] It was found that CdS grown on ZnO acts as a good interfacial layer between CdSe QDs and ZnO for effective charge carrier transport as well as facilitates smooth deposition of CdSe QDs on to the photoanode.[54,55]

Herein, we have synthesized porous hexagon shaped ZnO nanodisks (NDs) exposed in $\pm(0001)$ polar facets by utilizing ethyl cellulose (EC) as a capping agent and cetyltrimethylammonium bromide (CTAB) as a structure directing agent. We have explained the formation mechanism of as-synthesized ZnO NDs and evaluated their photovoltaic properties in CdS/CdSe-sensitized solar cells. Optimization of the ZnO NDs based solar cell performance regarding the CdSe QD deposition is carried out by varying the precursor concentration (the Cd:Se ratio) during the chemical bath deposition (CBD) process and compared the highest performing solar cell ($\eta \approx 4.86\%$) with the device fabricated with conventional ZnO NPs ($\eta \approx 3.14\%$), ZnO NRs ($\eta \approx 2.52\%$), and ZnO NSs ($\eta \approx 1.64\%$). Enhanced efficiency of the porous ZnO ND based photovoltaic device is due to efficient photoexcited charge separation and collection, better light scattering, and high surface area for sensitizer adsorption. Current−voltage (J−V), incident photon to current conversion efficiency (IPCE), and electrochemical impedance spectroscopy (EIS) measurements are employed to explain the characteristics of the photovoltaic devices.

2. EXPERIMENTAL SECTION

2.1. Materials. The chemicals and reagents used during this work are all analytically pure and used directly as received without further purification. They are, namely, zinc nitrate hexahydrate (Merck), ethyl cellulose (Himedia; ethoxy content, 48%), cetyltrimethylammonium bromide (Rankem), zinc chloride (Merck), sodium hydroxide (Himedia), cadmium nitrate hexahydrate (Merck), sodium sulfide (Merck), cadmium acetate (Merck), selenium powder (Merck), sodium sulfite (Merck), ammonium hydroxide (Merck), a triblock copolymer poly(ethylene glycol)-*block*-poly(propylene glycol)-*block*-poly(ethylene glycol) or PEG-PPG-PEG (Sigma-Aldrich), terpineol (Himedia), chloroplatinic acid (Sigma-Aldrich), 1-butanol (Merck), methanol (Merck), and ethanol (TMEDA). Fluorine doped tin oxide (FTO) coated glass substrates having sheet resistance of 8−10 $\Omega\ cm^{-2}$ are obtained from Sigma-Aldrich (St. Louis, MO, USA), used as substrates for both electrodes, and for all of the experiments high grade Milli-Q water (18.2 $M\Omega\ cm^{-2}$) is used.

2.1.1. Synthesis of ZnO Nanodisks. In a typical procedure, 1 g of EC is dissolved in 75 mL of 1-butanol (solvent) to get a clear solution (solution 1). A 25 mL aliquot of water (antisolvent) is then added to the solution 1 with constant stirring. A turbid colloidal dispersion of EC is obtained (solution 2). A 5 mmol (1.82 g) amount of cationic surfactant (i.e., CTAB) is then added to the solution and stirred for 5 min. Subsequently, zinc nitrate hexahydrate (5 mmol; 1.48 g) is added into solution 2, followed by dropwise addition of aqueous sodium hydroxide solution (10 mmol; 0.4 g) with continuous stirring, and the pH of the solution is found to be around 9−9.5. The resulting solution is then transferred into a 250 mL round-bottom flask, gradually heated to 100 °C, and refluxed for 10 h. After cooling to the room temperature, the resultant precipitate is centrifuged and washed with absolute ethanol and distilled water several times. The obtained product is dried in a hot air oven at 70 °C for 10 h. A pale white powder is formed which is calcined at 500 °C for 2 h in a muffle furnace to get the hexagon shaped mesoporous ZnO nanodisks. Reactions in the presence of only EC and only CTAB are also carried out separately, keeping the same reaction conditions in order to compare the influence of both of the additives.

2.1.2. Synthesis of ZnO Nanoparticles. ZnO NPs are synthesized by following a previously reported procedure.[56] To prepare ZnO nanoparticles, $ZnCl_2$ (1.1 g, 40 mmol) is dissolved in Milli-Q water (40.0 mL) and the solution is heated at 90 °C with constant stirring. Then 16 mL of 5 M aqueous NaOH solution is added slowly into the reaction mixture with stirring at the same temperature for another 30 min. The reaction mixture is allowed to cool to room temperature, and the precipitate is separated out by discarding the supernatant liquid. The precipitate is washed with distilled water several times for complete removal of NaCl, which is confirmed by $AgNO_3$ titration method. Further, purified particles are dispersed in isopropanol under an ultrasonic bath for 10 min at room temperature. The obtained product is centrifuged and dried in a hot air oven at 80 °C for 4 h. Finally the ZnO nanoparticles are obtained via calcination at 450 °C for 5 h in a muffle furnace.

2.1.3. Fabrication of Photoanodes and Devices. ZnO NDs based photoanodes are fabricated by preparing a homogeneous paste of as-synthesized ZnO ND powder (0.5 g) with a mixture of 2 mL of terpineol and 0.2 g of PEG-PPG-PEG in an agate mortar. This homogeneous paste is deposited on a precleaned conductive glass substrate, i.e., FTO via doctor blade technique, and the films are dried in air. After that these films are calcined at 480 °C for 30 min to remove the polymer. The thickness of the ZnO ND layer is measured by surface profilometer, and it is found to be in the range of 12−15 μm. The ZnO ND electrodes are co-sensitized with the CdS and CdSe. CdS QDs are deposited on ZnO via successive ionic layer adsorption and reaction (SILAR) process. In the SILAR method, first the electrodes are dipped into an ethanolic solution of $Cd(NO_3)_2\cdot 6H_2O$ (0.5 M) for 1 min, rinsed with ethanol, and dried on a hot plate at 70 °C. Again they are dipped into a Na_2S (0.5 M) solution in methanol for 1 min, rinsed with methanol, and dried at 70 °C. The amount of CdS grown onto the ZnO system is controlled by the number of repeated SILAR cycles. Chemical bath deposition (CBD) method is used for CdSe sensitization. For the CBD, various solutions having different precursor concentration ratios are prepared. At a fixed concentration of 5 mM $Cd(CH_3COO)_2 \cdot 2H_2O$, the Na_2SeSO_3 concentrations are set at 2.0,1.5, 1, and 0.5 mM in four different chemical baths from which four different CdSe deposited photoanodes are prepared and designated as Se [2.0], Se [1.5], Se [1] and Se [0.5], respectively. For deposition of CdSe QDs, the CdS-sensitized ZnO ND photoanodes are immersed in the aforementioned solutions with an added 75 μL of ammonium hydroxide for 3 h at 95 °C, and this procedure is repeated three times. Hereafter, the fabricated photoanode is represented as ZnO ND-CdS-CdSe (see Figure S1, Supporting Information (SI)). ZnO NPs, ZnO NRs and ZnO NSs based photoanodes are fabricated by following the same procedure used for ZnO NDs based photoanodes. In brief, the corresponding pastes are prepared by simple mixing and grinding of ZnO powder (0.5 g), terpineol (2 mL), and triblock PEG-PPG-PEG copolymer (0.2 g) in an agate mortar. The as prepared ZnO pastes are coated by using doctor blade technique over precleaned FTO substrates. These substrates are dried in air and then calcined at 450 °C for 30 min to get ZnO films with thickness ~ 12−15 μm, confirmed by the surface profilometer. For co-sensitization of CdS/CdSe, the same methods, i.e., SILAR (CdS) and CBD (CdSe), are employed. The photovoltaic devices are fabricated by sandwiching the photoanodes and counter electrodes. Electrolyte solution of sulfide/polysulfide ($S^{2-}/S_n^{\,2-}$) is added after sealing the device by using low temperature thermoplastic sealant, (thickness ~ 50 μm). The Pt counter electrodes are prepared by spin coating a solution of chloroplatinic acid (5 mM in isopropanol) on a precleaned FTO substrate followed by the calcination at 450 °C for (heating ramp of 5 °C/min) 30 min in a muffle furnace and cooled to room temperature naturally. $S^{2-}/S_n^{\,2-}$ electrolyte is prepared by dissolving 1 M sulfur powder, 1 M Na_2S, and 0.2 KCl in a solvent mixture of methanol−water (7:3, v/v). The active area for all fabricated devices is the same, and it is found to be ~0.25 cm^2. Before the photovoltaic measurements, the fabricated devices are kept under dark condition for 24 h.

2.1.4. Measurements and Material Characterization. The X-ray diffraction (XRD) measurements are taken by using Rigaku TTRAX-III X-ray diffractometer with Cu Kα (λ = 1.54 Å) with an operating voltage of 50 kV and current of 190 mA. The scan rate is fixed at 0.03°/s for taking the XRD patterns within the 2θ range of 10−80°. Brunauer−Emmett−Teller (BET) surface area analyses for all of the as-synthesized materials are carried out by nitrogen (N_2) adsorption at liquid N_2 temperature with a Beckman-Coulter SA 3100 N_2 adsorption apparatus. Samples are degassed at 150 °C for 2 h prior to surface area analysis. The UV−vis diffuse reflectance spectra (DRS) are recorded via a JASCO Model V-650 spectrophotometer by using a 150 mm integrating sphere, and $BaSO_4$ is used as an internal standard. The photoluminescence (PL) measurements were carried out using a Horiba−Jobin Yvon Fluoromax 4 spectrophotometer. The surface morphologies of the as-synthesized materials are investigated by field emission electron microscopy (FESEM) images, taken by using a Zeiss (Gemini) instrument. The transmission electron microscopy (TEM) measurements are carried out on a JEOL JEM 2100 microscope with an operating voltage of 200 kV. The thickness measurements of the photoanode films are carried out by using a Veeco Dektak-150 surface profilometer. The electrochemical impedance spectroscopy (EIS) measurements are performed by using a model CHI680E instrument from CH Instruments, Inc., Austin, TX, USA. A Keithley 2400 source meter is used for current density−voltage ($J-V$) measurements of the fabricated devices in the dark, and for light illumination, an AM 1.5G artificial solar simulator of 100 mW/cm^2 is used. A standard Si photovoltaic cell is used to calibrate the intensity of a 450 W arc lamp of Newport ORIEL Sol3A solar simulator. The incident to photon current conversion efficiencies (IPCE) of the fabricated devices are evaluated on a Newport ORIEL IQE-200 instrument fitted with a 250 W quartz tungsten halogen lamp calibrated by standard Si and Ge diodes.

3. RESULTS AND DISCUSSION

3.1. Powder X-ray Diffraction Analysis. Figure 1 shows powder X-ray diffraction (PXRD) patterns for all the synthesized products, i.e., ZnO before and after calcination, in the presence of both EC and CTAB (traces a and b), ZnO before and after calcination in the presence of only CTAB (traces c and d), and the precursor complex $Zn_5(OH)_8(NO_3)_2 \cdot 2H_2O$ before calcination (trace e) and for ZnO obtained after calcination, synthesized in the presence of only EC (trace f). The crystal phase for all of the ZnO is concluded as a hexagonal wurtzite phase with $(10\bar{1}0)$, (0002), $(10\bar{1}1)$, $(10\bar{1}2)$, $(11\bar{2}0)$, and $(10\bar{1}3)$ planes and a $P6_3mc$ space group symmetry according to JCPDS Card No. 36-1451. No peaks due to impurities are detected in the PXRD patterns of ZnO, and characteristic diffraction peaks become sharp and intense after calcination, indicating their improved crystalline nature. A precursor complex is formed when the reaction is carried out in the presence of only EC. The PXRD pattern of the ZnO precursor complex is well-matched with the diffraction pattern of $Zn_5(OH)_8(NO_3)_2 \cdot 2H_2O$ (JCPDS Card No. 25-1028). After calcination the precursor complex is converted into pure ZnO as confirmed from the PXRD pattern, trace f.

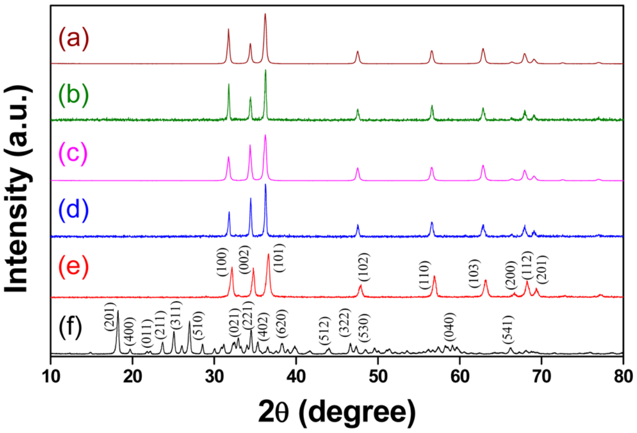

Figure 1. Powder X-ray diffraction (PXRD) patterns for as-synthesized ZnO before and after calcination in the presence of EC and CTAB (a and b), ZnO before and after calcination in the presence of only CTAB (c and d), the precursor complex $Zn_5(OH)_8(NO_3)_2 \cdot 2H_2O$ before calcination (e), and ZnO after calcination in the presence of only EC (f).

Figure 2A represents the intensity variation of PXRD peaks for $(10\bar{1}0)$, (0002), and $(10\bar{1}1)$ planes of ZnO synthesized in the presence of (a) both CTAB and EC, (b) only CTAB, and (c) only EC. All of the products are observed to be crystallized in the hexagonal wurtzite phase with a $P6_3mc$ space group symmetry. Note that the ratio of intensities from $(10\bar{1}0)$ and (0002) planes varied significantly, indicating a differential growth behavior of ZnO crystals in all of the three reaction conditions. A smaller value of $(10\bar{1}0)/(0002)$ ratio indicates the formation of ZnO rods showing a preferential (oriented) growth along the *c*-axis, whereas a larger value of $(10\bar{1}0)/(0002)$ ratio specifies inhibited growth along the *c*-axis, leading to the formation of disks as represented in Figure 2B.[27,29]

Figure 2C is a model representing atomic stacking of the wurtzite ZnO polar crystal in which O^{2-} and Zn^{2+} ions stack alternatively along the *c*-axis, resulting in Zn-terminated (0001) and O-terminated $(000\bar{1})$ planes with higher surface energy. Another group of semipolar planes $(10\bar{1}1)$ and nonpolar planes

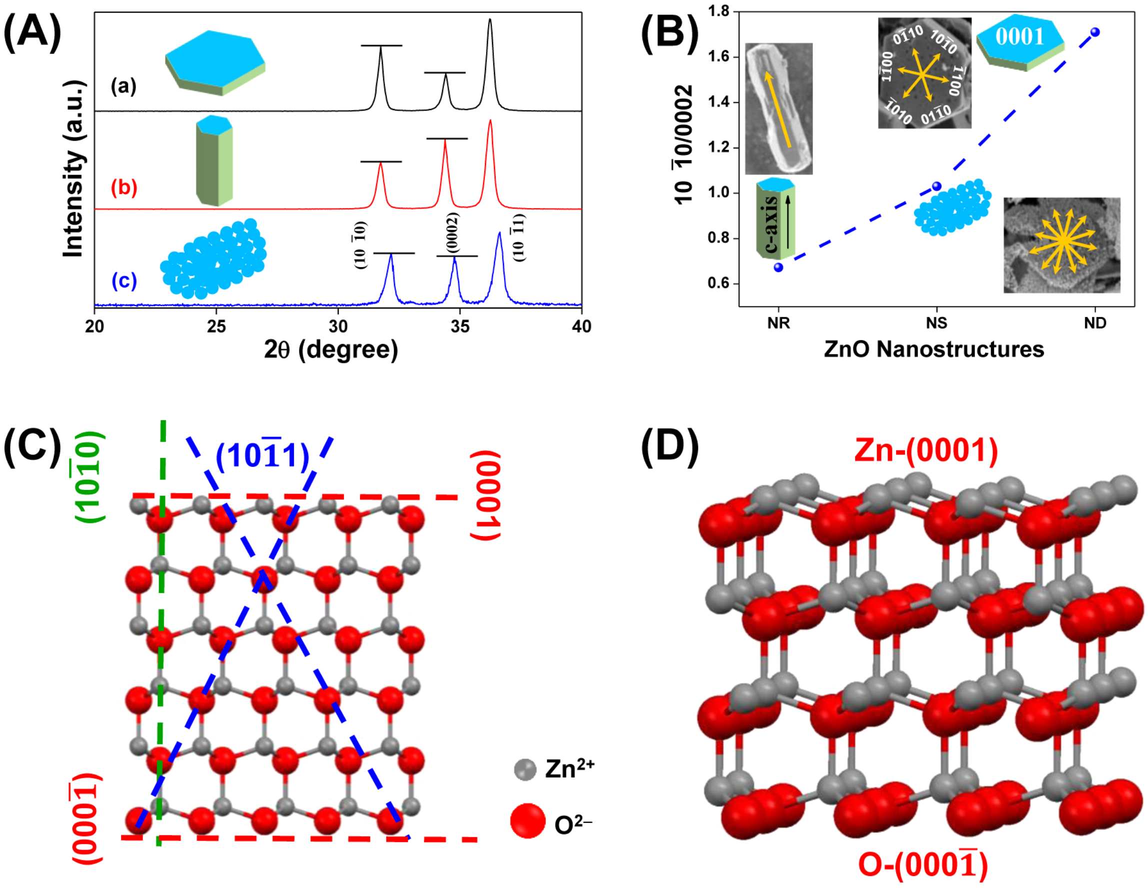

Figure 2. (A) Intensity variation of powder X-ray diffraction peaks for $(10\bar{1}0)$, (0002), and $(10\bar{1}1)$ planes of ZnO prepared in the presence of (a) CTAB and EC, (b) only CTAB, and (c) only EC. (B) Plot of the $(10\bar{1}0)/(0002)$ intensity ratio vs all of the ZnO nanostructures obtained under different reaction conditions along with a schematic illustration of the morphology models for nanorods (NR), nanosheets (NS), and nanodisks (ND), respectively. Inset shows FESEM images of a ZnO ND with crystal orientations along six symmetric directions, ZnO NS with random growth of crystal planes, and ZnO NR with preferential growth along the *c*-axis (0002 direction). (C) Two-dimensional atomic stacking model of wurtzite ZnO showing $\{\pm(0001), \pm(10\bar{1}0), \pm(10\bar{1}1)\}$ planes. (D) Three-dimensional atomic stacking model of wurtzite ZnO showing the Zn-terminated (0001) plane and the O-terminated $(000\bar{1})$ plane.

are $(10\bar{1}0)$, $(0\bar{1}10)$, and $(1\bar{1}00)$ in the wurtzite ZnO crystal. The nonpolar planes are composed of equivalent O^{2-} and Zn^{2+} ions and have the lowest surface energy.[28] It is known that, in general reaction conditions, ZnO prefers to grow along the *c*-axis with high energy polar ±(0001) facets, to minimize the high surface energy. Therefore, the polar (0001) and $(000\bar{1})$ planes are less exposed or disappear from these ZnO nanorod structures. But in the case of hexagon shaped ZnO crystals, a high percentage of polar surfaces are exposed due to the inhibited growth along the *c*-axis and favored growth along six symmetric directions of $\pm(0\bar{1}10)$, $\pm(10\bar{1}0)$, and $\pm(1\bar{1}00)$ as we have shown in the inset of Figure 2B. Figure 2D represents the 3-D atomic stacking model of wurtzite ZnO showing Zn-terminated (0001) and O-terminated $(000\bar{1})$ polar planes.

Figure 3 represents PXRD patterns for CdS and CdSe co-sensitized ZnO NDs (trace a), CdSe NPs (trace b), CdS NPs (trace c), and pristine ZnO NDs (trace d). All of the resolved diffraction peaks of CdS and CdSe in the diffraction pattern of CdS/CdSe co-sensitized ZnO ND photoanode (trace a) reveal successful deposition of cubic zinc blende CdSe (JCPDS no. 19-0191; trace b) and CdS (JCPDS no. 10-0454; trace c) QDs without any indication of crystalline impurities such as SeO_2, CdO, and so on. The average crystallite sizes of the CdS and CdSe QDs deposited on the photoanodes are estimated from the Debye−Scherrer equation and are found to be around ∼5.0−5.5 nm (see Table S2, SI). In addition, the diffraction peaks for pristine ZnO NDs can also be seen in the diffractogram for CdS/CdSe-sensitized photoanodes, which is

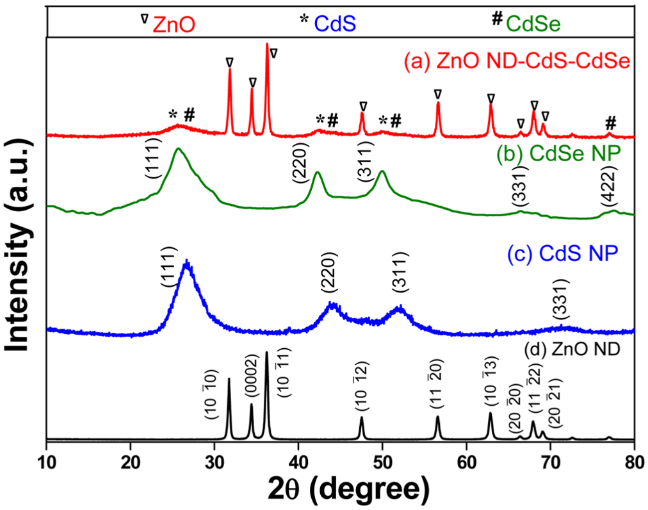

Figure 3. (a) CdS and CdSe co-sensitized ZnO NDs, (b) CdSe NPs, (c) CdS NPs, and (d) pristine ZnO NDs.

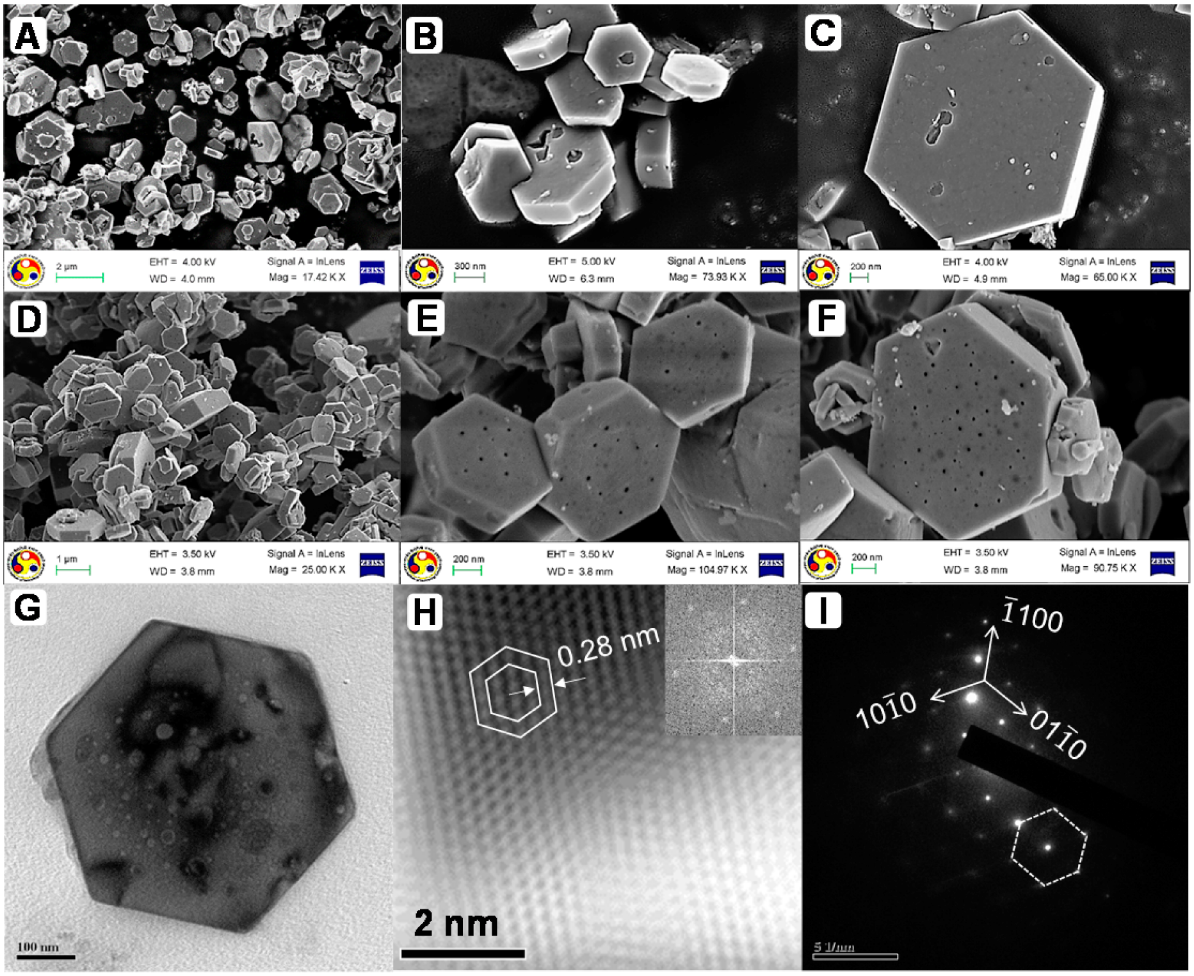

Figure 4. FESEM images of the ZnO NDs before calcination (A−C) and porous hexagonal ZnO NDs (D−F) after calcination at different magnifications. (G) TEM of a single ZnO ND. (H) HRTEM image of the ZnO ND, showing interplanar spacing, viewed along the [0001] direction with FFT in the inset. (I) SAED pattern of the ZnO ND, confirming its single crystalline nature.

symptomatic of the retention of crystal structure of ZnO ND even after sensitization processes.

3.2. Material Morphology. Figure 4 shows the FESEM features of as-synthesized hexagon shaped ZnO NDs before calcination (A−C) and after calcination (D−F). The average dimensions of the ZnO hexagons are in the range of 1−4 μm, and thicknesses are in the range of 70−100 nm. Before calcination the surface morphology of the ZnO NDs is observed to be smooth and nonporous while, after the calcination, ZnO NDs become porous. A distinct porous structure in ZnO NDs has been observed in the range of 5−10 nm, by FESEM as well as TEM analysis (panel G). It can be seen from inverse fast Fourier transform (IFFT) of atomic planes (trace H) of ZnO NDs that the arrangement of atoms is regular and forms a 6-fold symmetric projected structure. The interplanar distance of the lattice pattern is found to be ~0.28 nm which corresponds to the $(10\bar{1}0)$ lattice planes. This is indicative of favorable growth mainly along the six symmetric directions of the $\pm(10\bar{1}0)$, $\pm(1\bar{1}00)$, and $\pm(01\bar{1}0)$ lattice planes and suppression of typical growth along the [0001] direction.[57] The inset to trace H represents FFT, obtained from the HRTEM image, and accords with the diffraction pattern of the [0001] zone axis of ZnO. Figure 4I depicts the selected area electron diffraction (SAED) pattern of ZnO ND, when the electron beam was perpendicular to the nanodisk top facet which is recognized as the [0001] growth direction of ZnO. The ZnO ND is diffracting as a wurtzite single crystal and exhibits a hexagonally symmetrical pattern with [0001] zone axis, confirming dominant exposed facets are the polar ±[0001] planes which are top/bottom surfaces.[28]

The plausible mechanism of formation of ZnO nanodisks can be explained from Scheme 1.

EC is a derivative of cellulose, comprised of an anhydroglucose (cellulose) repeating backbone in which a high degree of hydroxy groups on the anhydroglucose are converted into ethyl ether groups. It is insoluble in water, is hydrophobic in nature, and has no native charge. Jin et al. reported that EC molecules in a solvent and antisolvent system (e.g., acetone:water) forms a turbid colloidal dispersion having an apparent charge due to hydroxyl ion adsorption induced by the solvent.[58] In the present study, we have also observed formation of a stable colloidal dispersion of EC molecules in a 1-butanol:water (3:1) solvent system (see images A and B, Scheme 1 and SI Figure S2). The ζ potential of the colloidal dispersion is found to be around −32 mV (reaction 1), while the net charge of the EC solution in 1-butanol is found to be almost zero. These negatively charged EC molecules are believed to electrostatically interact with the positively charged Zn^{2+} populated (0001) facets of polar ZnO during crystal growth and alter the crystal growth habits. CTAB is a cationic surfactant and completely

Scheme 1. Chemical Reactions Involved in Formation of Porous Hexagonal ZnO NDs and Digital Images (A and B) of EC Solutions in 1-Butanol and the 1-Butanol:Water (3:1) Solvent System

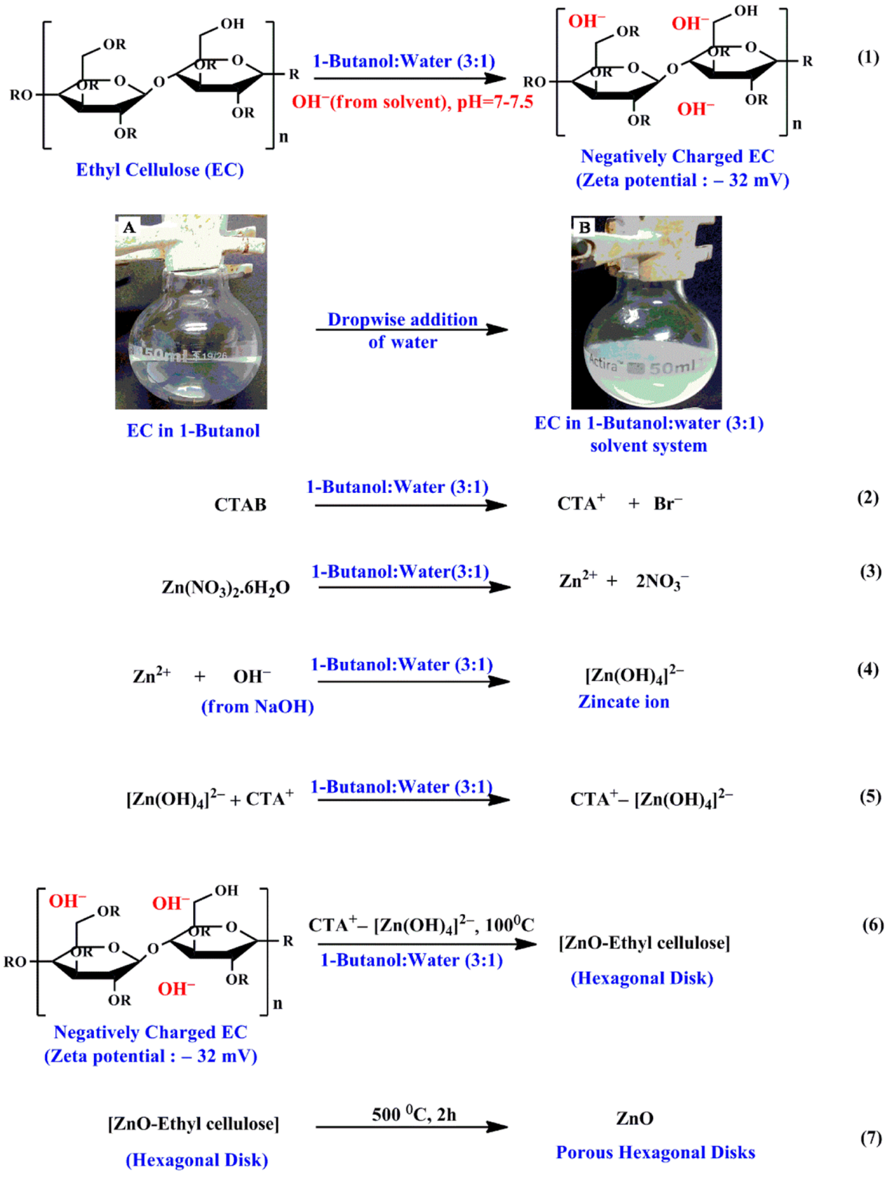

ionizes in water as shown in reaction 2, Scheme 1. It is well-known that zinc nitrate ionizes in aqueous solutions and zinc cations readily react with hydroxide anions in basic reaction conditions to form stable tetrahedral $Zn(OH)_4^{2-}$ complexes which act as the growth units for various ZnO structures (reactions 3 and 4). In the presence of CTA^+ ions, negatively charged zincate ions form $CTA^+{-}Zn(OH)_4^{2-}$ ion pairs due to their electrostatic interactions (reaction 5). Previously, Sun et al. had reported that CTA^+ ions can serve as a carrier for negative zincate [i.e., $Zn(OH)_4^{2-}$] and organizes the growth process of ZnO nanorod.[59] Additionally, CTAB molecules decrease the surface tension of the solution which decreases the energy needed to form a new phase. In the present reaction conditions, it is believed that the nucleation of ZnO from zincate ions is organized by CTA^+ ions, while the negatively charged EC molecules provide adsorption sites for the ZnO growth units, i.e., $CTA^+{-}Zn(OH)_4^{2-}$ ion pairs, and adhere preferentially on the Zn^{2+} populated (0001) crystal surface to impede the CTAB assisted favorable *c*-axis growth of ZnO crystal and leads to the formation of hexagonal disk shaped ZnO (reaction 6). After calcination in air at 500 °C the EC molecules decompose and escape as CO_2 and H_2O from the ZnO hexagonal disks to develop pores (reaction 7).

We have synthesized ZnO in the presence of only CTAB and have kept the other reaction conditions unchanged as we have followed for the synthesis of ZnO NDs. Interestingly, we have not observed any formation of pores in this case even after calcination at 500 °C for 2 h, and the shape of ZnO in this condition is observed to be a hexagonal nanorod (Figure 5A−C) as predicted from the PXRD pattern (see Figure 2). This confirms that EC molecules are not only responsible for pore formation but also inhibiting growth of ZnO along the direction of the *c*-axis leading to a high percentage exposure of active ±(0001) polar facets.

Panels D−F of Figure 5 represent FESEM images of ZnO synthesized in the presence of only EC, and the formation of ZnO nanosheets composed of numerous nanoparticles are noted in this instance. This may be due to random arrangement and

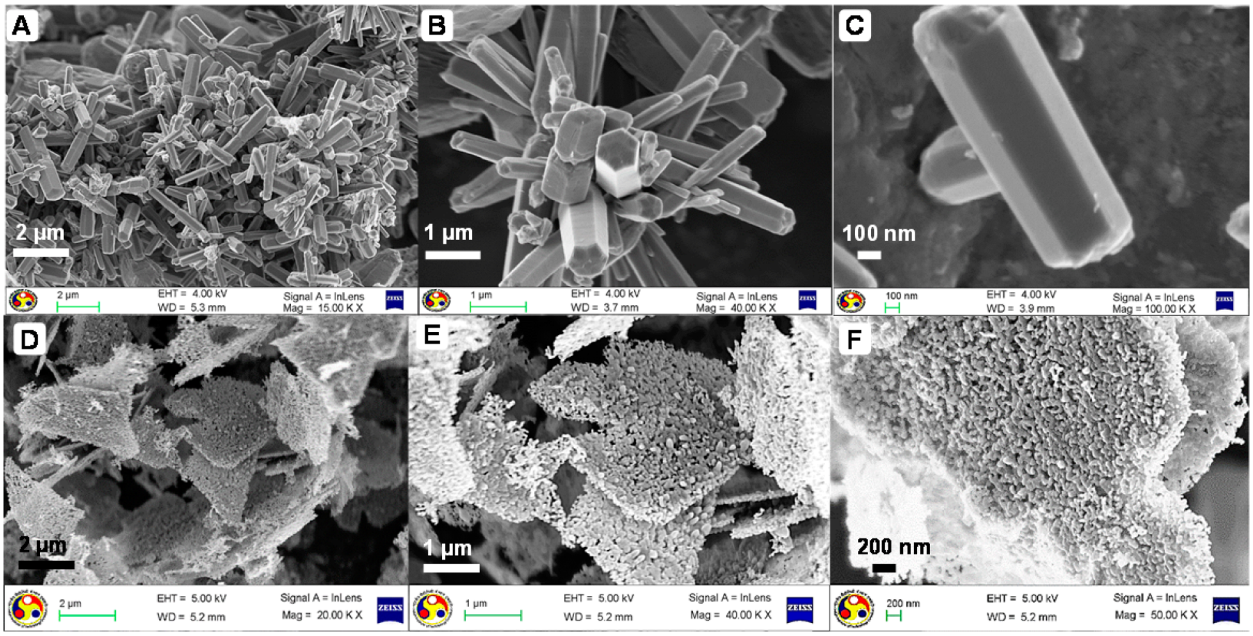

Figure 5. FESEM images of the ZnO NRs (A−C) and porous ZnO NSs (D−F) after calcination at different magnifications prepared in the presence of only CTAB and only EC, respectively.

Scheme 2. Schematic Representation of Synthetic Routes of ZnO Nanodisks (NDs) (Path 1), Nanorods (NRs) (Path 2), and Nanosheets (NSs) (Path 3) under Three Different Reaction Conditions

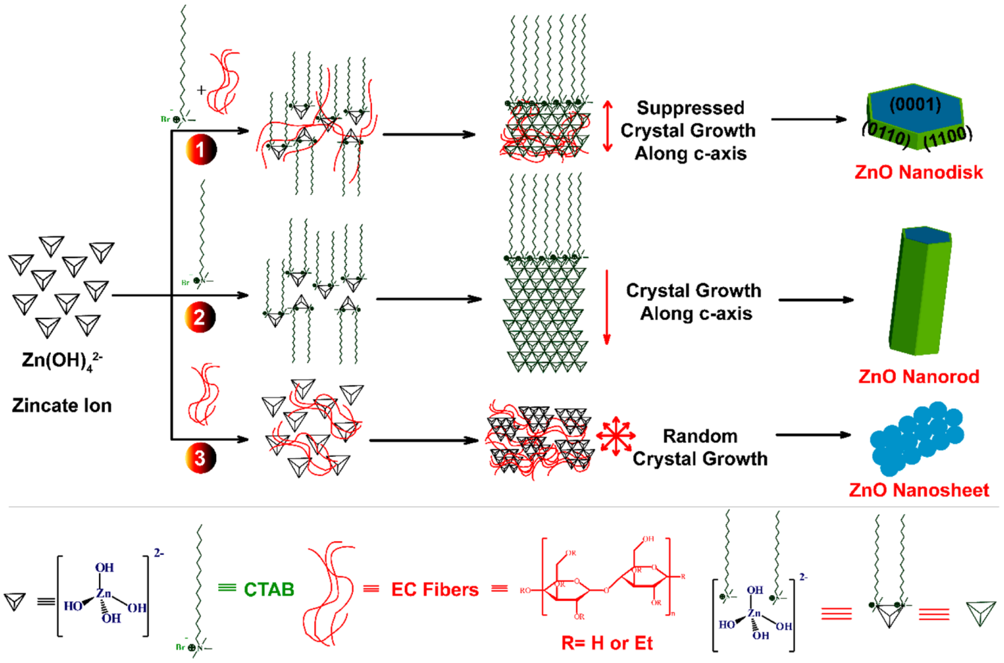

adsorption of the growth units (i.e., zincate or $Zn(OH)_4^{2-}$) onto the EC fibers (Scheme 2). This observation divulges that hexagon shape growth of ZnO is encouraged by only CTAB molecules in the reaction mixture. Hence, the CTAB molecules are acting as a structure directing agent while the EC molecules are acting as a capping agent in the reaction system. Formation of all of the ZnO heterostructures obtained under different reaction conditions are schematically represented in Scheme 2.

3.3. UV−Visible Absorption and Photoluminescence Analysis. Figure 6A represents UV−vis absorption spectra for all of the ZnO heterostructures, i.e., ZnO NS (black line), ZnO NR (red line), and ZnO ND (blue line). We have observed a moderate blue shift of absorption onset in the case of ZnO NS (~25 nm) and ZnO NR (~20 nm) as compared to the ZnO ND. This may be due to the smaller size of ZnO nanoparticles in ZnO NS and the smaller size distribution of ZnO NR as compared to ZnO NDs. The inset to Figure 6A depicts corresponding Tauc's plots to estimate the band gap values of allof the samples, where $(\alpha h\nu)^2$ is plotted against the photon energy ($h\nu$) and α is the absorption coefficient. The band gap values of ZnO heterostructures are estimated as 3.21 eV for ZnO NS, 3.18 eV for ZnO NR, and 3.15 for ZnO ND. The observed lowering of band gap values for ZnO NR and ZnO ND in contrast to ZnO NS is in accordance with the blue shift

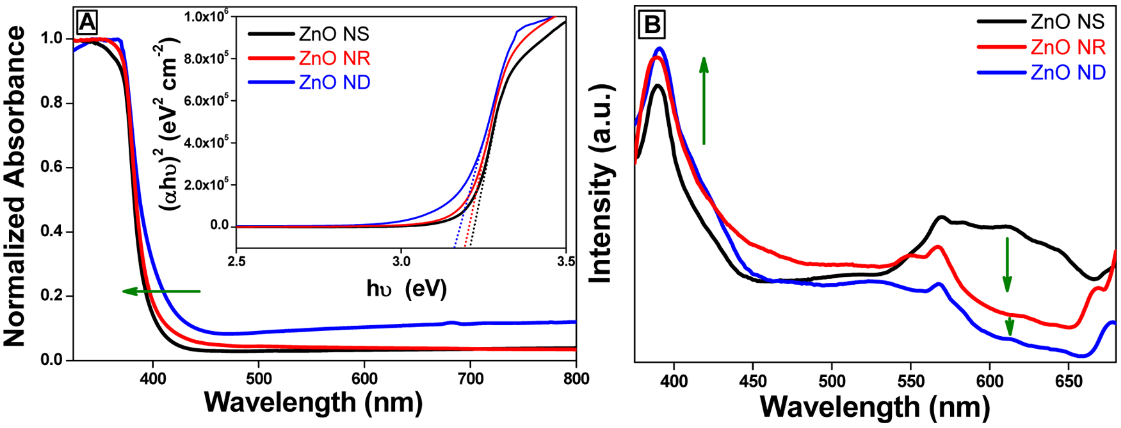

Figure 6. (A) UV–visible absorption profile for all of the ZnO heterostructures (ZnO NS, ZnO NR, and ZnO ND). Inset shows corresponding Tauc's plots to estimate optical band gap values. (B) Steady state photoluminescence spectra for all of the ZnO heterostructures.

of absorption profiles. The room temperature steady state PL spectra of ZnO with different morphologies are carried out in order to analyze their emission characteristics, defect states, and crystal quality as shown in Figure 6B. For all of the samples sharp emissions in the UV range (~380 nm) and broad emission bands in the visible region (~580–680 nm) are observed. The sharp emission in the UV range is the near-band-edge emission and arises due to radiative exciton recombination while the emission peaks observed in the visible region are attributed to defect states in the ZnO crystal structure in which oxygen vacancies are the most probable source.[60,61] From Figure 6B, it is clear that the intensity of near-band-edge emission increases as ZnO NS < ZnO NR < ZnO ND while the intensity of the broad emission band in the visible region is maximum for ZnO NS and gradually decreases from ZnO NR to ZnO ND. This is a clear reflection of minimum defect sites in ZnO ND and ZnO NR than in ZnO NS which is beneficial for efficient photoinduced charge migration followed by collection in photovoltaic devices. It should be noted that ZnO NSs are composed of numerous interconnected ZnO NPs, for which the probability of population of grain boundary induced defect sites will be maximum and is consistent with the PL analysis. Further, we have carried out PL analysis of ZnO nanodisks (NDs) and ZnO nanorods (NRs) before calcination and compared with the spectra obtained after calcination (see Figure S3, SI). After calcination, the near-band-edge emission peaks (~380 nm) for both of the ZnO heterostructures become sharper. In addition, the satellite peaks observed in the range of 420–500 nm originating from the coordinatively unsaturated Zn^{2+} interstitial sites (Zn_i, shallow donor) in the ZnO nanostructures have disappeared. The intensity of broad emission bands in the visible region (~550–650 nm), attributed to the transition from the conduction band to the deep trap levels of ZnO (created by oxygen vacancies in the ZnO crystal structure), are also observed to be reduced after calcination. The aforementioned points are indicative of the reduction of intrinsic defect levels (both Zn_i and oxygen vacancies) of ZnO (ND and NR) heterostructures after calcination.

3.3. BET Surface Area Analysis. BET surface area analyses of all of the as-prepared ZnO with different morphologies are shown in Figure 7. The desired characteristics of a wide band gap semiconductor (i.e., photoanodic materials) to be used in QSSCs in order to achieve better photovoltaic performance is that it should have (i) a high surface area and (ii) a highly porous nature. The observed BET surface area of the as-synthesized ZnO NS is found to be ~83 m^2 g^{-1}, for ZnO NPs is 52 m^2 g^{-1}, for ZnO ND is ~46 m^2 g^{-1}, and for ZnO NR is ~18 m^2 g^{-1}. From the Barrett–Joyner–Halenda (BJH) pore size distribution curves (inset to Figure 7), we have observed that the pore size distribution for ZnO NS is ~7–16 nm and for ZnO ND is ~5–8 nm, while there is no indication of pores in the case of ZnO NRs and ZnO NPs.

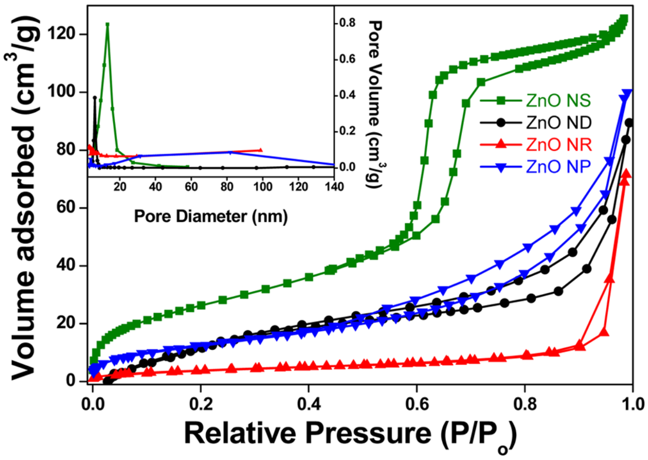

Figure 7. Nitrogen adsorption–desorption isotherms and Barrett–Joyner–Halenda (BJH) pore size distribution plots (inset) for as-synthesized ZnO nanosheets, hexagon shaped ZnO nanodisks, ZnO nanorods, and ZnO nanoparticles.

3.4. UV–Visible Absorption and Diffuse Reflectance Analysis of the Photoanodes. Figure. 8 represents the normalized UV–vis diffuse reflectance spectra (DRS) of pristine ZnO ND film and CdS/CdSe co-sensitized ZnO NDs photoanodes with different Se precursor concentrations (0.0, 0.5, 1.0, 1.5, and 2.0 mmol). The scan range is 200–800 nm for all of the samples and recorded against blank FTO as a reference. The characteristic absorption spectrum of ZnO NDs (blue line) shows a steep absorption edge at ~380 nm. It is well-known that nanocrystalline CdS QDs absorb photon energy in the region 380–520 nm while the CdSe QDs expand the absorption edge up to 750 nm. From Figure 8 we have seen that all of the photoanodes absorb from UV as well as in the visible region, confirming the roles of all of the components, i.e., ZnO, CdS, and CdSe. With the increase in precursor concentration of Se in the CBD process, the quantity of deposited CdSe QDs is increased in the photoanodes and absorption

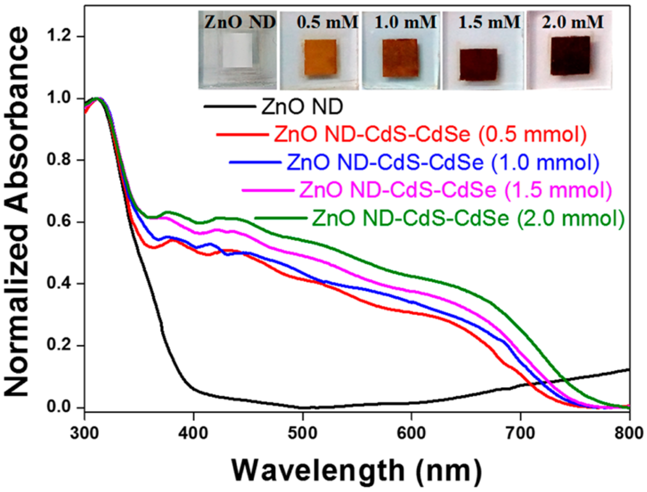

Figure 8. UV–vis diffuse reflectance spectra of CdS/CdSe co-sensitized ZnO ND based photoanodes with different Se precursor concentrations during the chemical bath deposition (CBD) methods. Inset shows the digital photographs of all of the photoanodes.

onsets are red-shifted from 700 to 750 nm. The observed red shifting of the absorption onset is due to the subsequent growth of CdSe QDs;[62] thus the light absorbance of ZnO ND-CdS-CdSe photoanode prepared with 2 mM Na_2SeSO_3 is found to be higher than those of the other samples due to its increased QD loading. The digital photograph of each sample (Figure 8) also indicates the gradual change in color from light brown to dark red with the increase in Se concentration demonstrating increased loading of CdSe QDs.

Figure 9 represents the diffuse reflectance spectra of ZnO NR, ZnO ND, ZnO NS, and ZnO NP based films deposited on FTO substrates. Diffuse reflectance measurements are carried out to compare the light-scattering properties of both of the films. The ZnO NR film exhibits much higher reflectance in the wavelength range 420–800 nm than that of the ZnO ND, ZnO NS, and ZnO NP based films. This is an indication of the higher light-scattering ability of ZnO NR photoanode as compared to the ZnO ND, ZnO NS, and ZnO NP based photoanodes.[6,63]

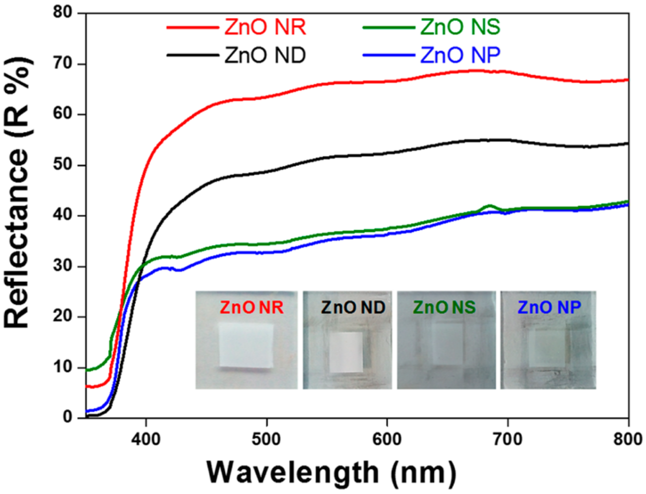

Figure 9. Diffuse reflectance spectra of the ZnO NR, ZnO ND, ZnO NS, and ZnO NP based films of similar thickness on FTO substrates. Insets show the digital photographs of the films.

3.5. Photovoltaic Characteristics of the Solar Cells.

Figure 10A shows the current density–voltage (J–V) characteristics of the CdS/CdSe co-sensitized ZnO ND based solar cells for optimization of CdSe QD loading under AM 1.5G simulated sunlight with a light intensity of 100 mW cm^{-2}. The photovoltaic parameters such as short-circuit current density (J_{sc}), open-circuit voltage (V_{oc}), fill factor (FF), and the overall power conversion efficiency (PCE, η) of all devices are listed in Table 1.

From Table 1, we have observed that device a based on the photoanode with ZnO ND-CdS-CdSe (1.5), i.e., CdSe deposition with Se precursor solution of 1.5 mM concentration, exhibits a maximum PCE ~ 4.86% and the lowest PCE (~2.83%) is observed for the device based on the photoanode ZnO ND-CdS-CdSe (0.5) which is due to low CdSe QD loading. For the devices a, c, and d with photoanodes ZnO ND-CdS-CdSe (1.5) [$J_{sc} \approx 16.0$ mA/cm^2], ZnO ND-CdS-CdSe (1.0) [$J_{sc} \approx 12.0$ mA/cm^2], and ZnO ND-CdS-CdSe (0.5) [$J_{sc} \approx 10.1$ mA/cm^2], respectively, as the amount of CdSe deposition increases, the J_{sc} values are also increasing consistently. But for device b, with ZnO ND-CdS-CdSe (2.0) photoanode, the J_{sc} value drops to ~13.7 mA/cm^2 and consequently decreases the PCE value to ~4.15%, possibly due to agglomeration of CdSe QDs with an increase in QD loading which increases recombination of the photoinduced electron in the photoanode. Additionally, the formation of crystalline impurities such as SeO_2, CdO, and so on in the ZnO ND-CdS-CdSe (2.0) photoanode are being probed, which can quench the J_{sc} value, by powder X-ray diffraction (PXRD) analysis. A comparison of the photoanode material to that of the PXRD pattern of ZnO ND-CdS-CdSe (1.5) photoanode has been given in Figure S4 (SI). No detectable impurity peaks are observed in the PXRD pattern of ZnO ND-CdS-CdSe (2.0). This result accords with our claim that J_{sc} decreases in the device with ZnO ND-CdS-CdSe (2.0) photoanode mainly due to agglomeration of CdSe QDs. A schematic presentation of charge recombination in the ZnO ND-CdS-CdSe (2.0) photoanode as compared to the ZnO ND-CdS-CdSe (1.5) photoanode is illustrated in Scheme S1 (SI).

Figure 10B illustrates the incident photon-to-current conversion efficiency (IPCE) as a function of wavelength for all of the fabricated QSSCs. The increase in J_{sc} values for the devices, following the order d < c < b < a, is also explicit in the IPCE plot, exhibiting the highest value up to ~80% in the wavelength range from 450 to 700 nm. From Figure 10B, it is obvious that the IPCE for the device ZnO ND-CdS-CdSe (1.5) is maximum (~80–70%) which indicates minimum photo-induced electron recombination and better light harvesting ability than the other three devices: i.e., ZnO ND-CdS-CdSe (2.0), ~70–60%; ZnO ND-CdS-CdSe (1.0), ~70–55%; and ZnO ND-CdS-CdSe (0.5), ~60–40%. This observation concludes that the optimal loading of CdSe QDs in ZnO ND-CdS-CdSe is 1.5 in the photoanode for a better light harvesting.

In order to ensure the superiority of ZnO NDs in photovoltaic application, we have compared the photovoltaic parameters of the highest performing solar cell device, i.e., device a of ZnO ND-CdS-CdSe (1.5), with a similar type of device fabricated with conventional ZnO NPs, as-synthesized ZnO NRs and ZnO NSs. Figure 11A represents characteristic current J–V curves for optimized CdS/CdSe co-sensitized ZnO ND, ZnO NP, ZnO NR, and ZnO NS based devices. Figure 11B shows IPCE plots for the respective devices.

The photovoltaic parameters such as J_{sc}, V_{oc}, FF, and η for all of the fabricated devices are listed in Table 2.

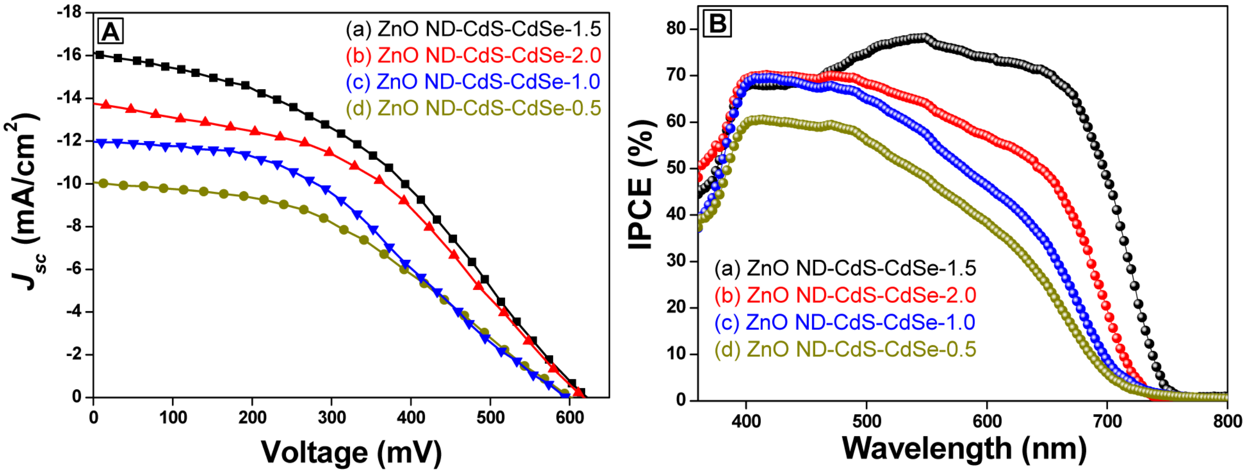

Figure 10. (A) Current density−voltage (J−V) curves for the photovoltaic devices (a) ZnO ND-CdS-CdSe (1.5), (b) ZnO ND-CdS-CdSe (2.0), (c) ZnO ND-CdS-CdSe (1.0), and (d) ZnO ND-CdS-CdSe (0.5) under AM 1.5 G solar illumination. (B) IPCE plots for the respective devices employing S^{2-}/S_n^{2-} as the redox couple.

Table 1. Short-Circuit Current Density (J_{sc}), Open-Circuit Voltage (V_{oc}), Fill Factor (FF), and Power Conversion Efficiency (η) for the Fabricated Solar Cells Incorporating Different Photoanodes

device	J_{sc} (mA/cm^2)	V_{oc} (mV)	FF (%)	η (%)	redox couple
(a) ZnO ND-CdS-CdSe (1.5)	16.0 (15.8 ± 0.6)	620 (615 ± 26)	49 (47 ± 2.5)	4.86 (4.55 ± 0.33)	S^{2-}/S_n^{2-}
(b) ZnO ND-CdS-CdSe (2.0)	13.7 (13.2 ± 0.5)	619 (615 ± 25)	48 (47 ± 1.4)	4.15 (4.05 ± 0.27)	S^{2-}/S_n^{2-}
(c) ZnO ND-CdS-CdSe (1.0)	12.0 (11.8 ± 0.4)	595 (570 ± 25)	45 (44 ± 1.3)	3.21 (3.10 ± 0.25)	S^{2-}/S_n^{2-}
(d) ZnO ND-CdS-CdSe (0.5)	10.1 (9.5 ± 0.6)	602 (575 ± 33)	47 (46 ± 1.8)	2.83 (2.65 ± 0.24)	S^{2-}/S_n^{2-}

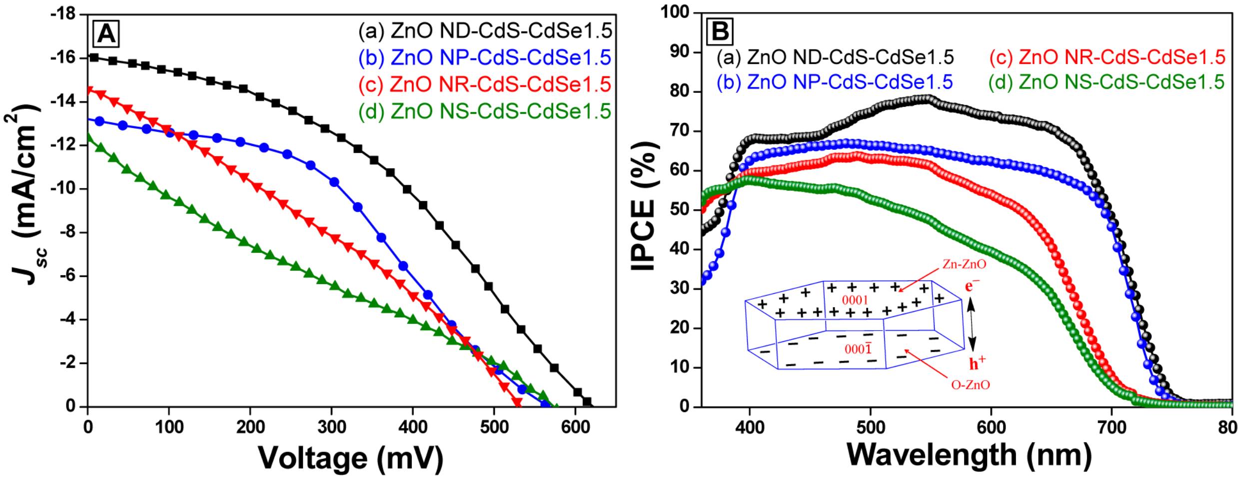

Figure 11. (A) Current density−voltage (J−V) curves for the photovoltaic devices (a) ZnO ND-CdS-CdSe (1.5) [black line], (b) ZnO NP-CdS-CdSe (1.5) [blue line], (c) ZnO NR-CdS-CdSe (1.5) [red line] and (d) ZnO NS-CdS-CdSe (1.5) [olive line] (B) IPCE plots for the respective devices employing S^{2-}/S_n^{2-} as the redox couple. Inset shows schematic illustration of charge separation model between polar Zn-populated (0001) [i.e., Zn-ZnO] and O-populated ($000\bar{1}$) [i.e., O-ZnO] surfaces.

Table 2. Short-Circuit Current Density (J_{sc}), Open-Circuit Voltage (V_{oc}), Fill Factor (FF), and Power Conversion Efficiency (η) for the Fabricated Solar Cells Incorporating Different Photoanodes

device	J_{sc} (mA/cm^2)	V_{oc} (mV)	FF (%)	η (%)	redox couple
(a) ZnO ND-CdS-CdSe (1.5)	16.0 (15.8 ± 0.6)	620 (615 ± 26)	49 (47 ± 2.5)	4.86 (4.55 ± 0.33)	S^{2-}/S_n^{2-}
(b) ZnO NP-CdS-CdSe (1.5)	13.2 (13 ± 0.5)	567 (550 ± 20)	42 (41 ± 2.3)	3.14 (3.12 ± 0.15)	S^{2-}/S_n^{2-}
(c) ZnO NR-CdS-CdSe (1.5)	14.6 (14 ± 0.8)	534 (520 ± 20)	32 (30 ± 2.3)	2.52 (2.40 ± 0.15)	S^{2-}/S_n^{2-}
(d) ZnO NS-CdS-CdSe (1.5)	12.4 (11.6 ± 1.0)	577 (550 ± 28)	23 (20 ± 4)	1.64 (1.50 ± 0.2)	S^{2-}/S_n^{2-}

From Figure 11A,B, higher J_{sc} values and IPCE of the ZnO ND based device in contrast to the ZnO NP, ZnO NR, and ZnO NSs based devices indicate better absorption of solar irradiation by the ZnO ND based photoanode probably due to better photoinduced charge separation and collection. In principle the IPCE of a solar cell is dependent on (i) the light

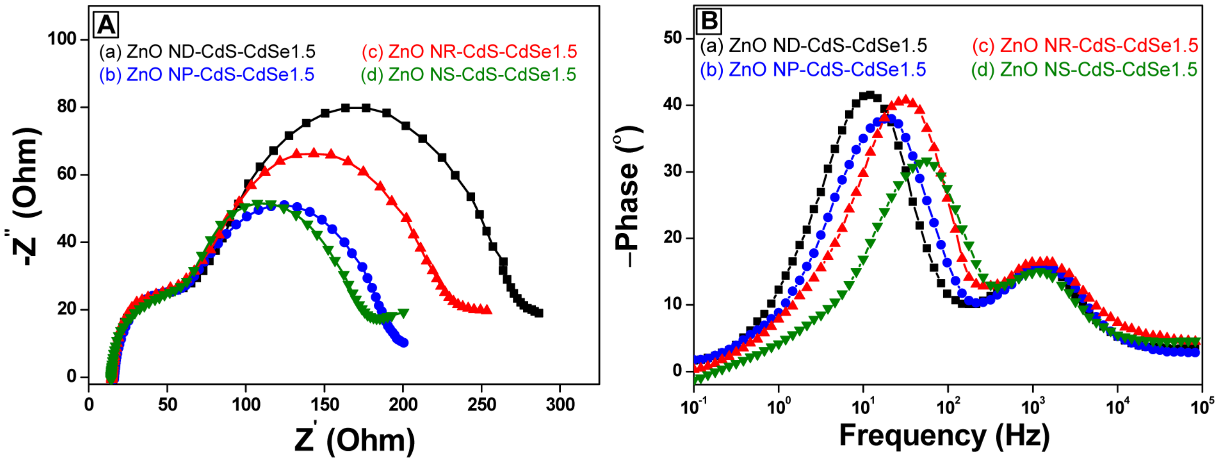

Figure 12. (A) Nyquist plots for photovoltaic devices (a) ZnO ND-CdS-CdSe (1.5) [black line], (b) ZnO NP-CdS-CdSe (1.5) [blue line], (c) ZnO NR-CdS-CdSe (1.5) [red line], and (d) ZnO NS-CdS-CdSe (1.5) [olive line] in the dark at open-circuit voltage and in a frequency range from 0.1 Hz to 100 kHz. (B) Bode phase plots for the respective devices.

harvesting efficiency, (ii) the quantum yield of electron injection, and (iii) the efficiency of collecting injected electrons.[64] The better light harvesting ability of the ZnO ND based device is attributed to the enhanced light confinement (over ZnO NP and ZnO NS based photoanodes) in the photoanode and efficient sensitization with CdS and CdSe QDs boosted by high surface area (~46 $m^2\ g^{-1}$), which upsurges the flux of photoinduced electron injection for an esteemed value of $J_{sc} \approx 16$ mA cm^{-2}. From Table 2, an appreciated value of J_{sc} for the ZnO NR based device (~14.6 mA cm^{-2}) is observed relative to that of the ZnO ND based device (~16.0 mA cm^{-2}). This is mainly due to high crystallinity and minimum intrinsic defect sites in the ZnO nanorods as evident from the PXRD pattern and PL analysis. Additionally, the higher light-scattering ability of the ZnO NR based photoanode is noted than that of the ZnO ND based photoanode (see Figure 9), which contributed toward an elevated value of short-circuit density. Derived V_{oc} and FF of the ZnO NP (~567 mV and ~42%, respectively), ZnO NR (~534 mV and ~32%, respectively), and ZnO NS based devices (~577 mV and ~23%, respectively) as compared to the ZnO ND based device (~620 mV and ~49%, respectively) are indicative of inferiority in efficient charge separation and regeneration of oxidized sensitizer particles. The enhanced charge separation in the ZnO ND based device can be well-explained with the help of a charge separation model between reactive polar Zn-populated (0001) [i.e., Zn-ZnO] and O-populated ($000\bar{1}$) [i.e., O-ZnO] surfaces; proposed by Chen et al.[65] as depicted in the inset to Figure 11B on the basis of periodic DFT calculations. Since ZnO ND is a polar single crystal with exposed Zn^{2+}-populated (0001) and O^{2-}-populated ($000\bar{1}$) surfaces, an internal electric field is expected to be generated between the two planes due to spontaneous polarization. When ZnO NDs are employed as a photoanodic material in the solar cell devices, the photoinjected electrons from the sensitizer particles, i.e., CdS and CdSe, will be migrated toward positive polar (0001) Zn-ZnO surfaces under the internal electric field and diffused through the photoanode film to the external circuit. Additionally, the single crystalline nature of the ZnO ND, with less intrinsic defect sites, facilitates the photoinduced electron diffusion process in the photoanode and enhances the charge separation to increase V_{oc} and FF of the device. As a consequence, the ZnO ND based device is furnishing a PCE value of ~4.86%, while ~3.14% is obtained for ZnO NP and ~2.52% for ZnO NR based devices. It is noteworthy that the surface area of ZnO NS (~83 $m^2\ g^{-1}$) is higher than those of ZnO NP (~52 $m^2\ g^{-1}$), ZnO ND (~46 $m^2\ g^{-1}$), and ZnO NR (18 $m^2 g^{-1}$), and hence the expected trend of sensitizer particle loading will be ZnO NS > ZnO NP > ZnO ND > ZnO NR. However, we have observed that the absorption intensity in the visible region is highest for ZnO NP and lowest for ZnO NS based photoanodes [see Figure S5, SI], which implies the actual trend of sensitizer particle loading is ZnO NP > ZnO ND > ZnO NR > ZnO NS. The probable explanation for this observation is the layered structure of ZnO NSs (see Figure 5D–F and Figure S6 of the SI), which causes minimum pore formation due to interparticle stacking in the photoanode. It should be pointed out that ZnO NSs are composed of numerous interlinked ZnO nanoparticles with a number of pores (i.e., intraparticle pores). After deposition of optimum CdS QDs, both the intraparticle and interparticle pores are clogged and inhibit the diffusion of CdSe QDs in the film during the sensitization process. Consequently, minimum deposition of CdSe QDs in the ZnO NS based photoanode is observed. This claim is also supported by the poor value of FF observed for the ZnO NS (~23%) based device as compared to those of ZnO ND (~49%), ZnO NP (~42%), and ZnO NR (~42%) based devices, which reflects slower regeneration of sensitizer particles by the redox couple in the ZnO NS based device. This may be caused by minimum available pores in the ZnO NS based photoanode for electrolyte diffusion relative to the ZnO ND, ZnO NP, and ZnO NR based photoanodes. It is well-known that the value of FF depends on sensitizer particle regeneration kinetics by the redox couple and photoinduced charge separation in the device.

Further, to gain insights into the electron transport and recombination kinetics in the photovoltaic devices, namely, (a) ZnO ND-CdS-CdSe (1.5), (b) ZnO NP-CdS-CdSe (1.5), (c) ZnO NR-CdS-CdSe (1.5), and (d) ZnO NS-CdS-CdSe (1.5), electrochemical impedance spectroscopy (EIS) is employed as shown in Figure 12A,B, obtained under darkness in a frequency range from 0.1 Hz to 100 kHz at the applied bias equivalent to the open-circuit voltages. From Figure 12A it is observed that all Nyquist plots are composed of two semicircles: the one in the medium-frequency region (right semicircle) is due to the charge-transfer process at the working electrode/electrolyte interface while another in the high-frequency region (left semicircle) is attributed to the redox reaction at the counter electrode/electrolyte interface.[66] As can be seen from Figure 12A, the diameter (R_k) of the right semicircle for the ZnO ND based device is larger relative to that of all other devices, and the increasing trend of R_k is ZnO NS < ZnO NP < ZnO NR < ZnO ND. It is well-known that R_k is mainly determined by the charge recombination resistance with partial contribution from transport resistance.[55] A large value of R_k for ZnO ND based device implies retarded backward reaction of QD injected electron at the ZnO ND/CdS-CdSe/electrolyte interface or lesser interfacial charge recombination with holes of the electrolyte in the device. This observation supports our claim of faster and efficient charge transport through the single crystalline ZnO NDs in the entire photoanode due to its single crystalline and exposed polar facets which is causing higher FF for the device (∼49%). Moreover, the photovoltaic devices behave like a diode on the applied bias voltage; R_k is considered as a part of shunt resistance (R_{sh}).[19] The relation between R_{sh} and FF can be expressed by the following equation:

$$\mathrm{FF} = \mathrm{FF}_0(1 - 1/R_{sh})$$

where FF_0 is the theoretical maximum FF. It can be expected that as a result of an increase in R_{sh} in the QSSC assembled with the ZnO NDs, a larger value of FF is perceived. On the other hand, the effect of charge separation boosted by exposed polar facets in ZnO NR based devices is minimum for which the observed charge recombination resistance is lesser than the ZnO ND based devices. Similarly, in the case of ZnO NP and ZnO NS devices the photoinduced electrons interact repeatedly with the traps in the grain boundaries as they undertake a random movement throughout the film. As a consequence, recombination reactions in these two photoanodes (ZnO NP and ZnO NS) become more prominent than in the ZnO ND based photoanode which is reflected in the derived values of FF and V_{oc} for the devices.

The Bode phase plots for all of the fabricated devices are presented in Figure 12B. The characteristic peak frequencies in the medium-frequency region (f_{max}) for the ZnO NS, ZnO NR, and ZnO NP based devices are located at ∼56.2, ∼31.6, and ∼21.5 Hz while that for the ZnO ND based device is found to be ∼12.1 Hz. We have calculated the photoinduced electron lifetimes (τ_e) in the CB of ZnO NS, ZnO NR, ZnO NP, and ZnO ND by using the formula $\tau_e = 1/(2\pi f_{max})$,[67] and they are found to be ∼2.8, ∼5.0, ∼7.4, and ∼13.1 ms, respectively. The increase in electron lifetime further confirms minimized photoinduced electron interception to the S^{2-}/S_n^{2-} redox shuttle in the ZnO ND device than all other devices. As a result, photoinduced electron density in the CB level of ZnO ND increases, leading to a higher value of J_{sc} which is contributed toward an increased trend of η of the devices.

CONCLUSIONS

We have developed a synthetic protocol for mesoporous hexagonal ZnO NDs with exposed ±(0001) polar facets utilizing ethyl cellulose (EC) and cetyltrimethylammonium bromide (CTAB) as capping and structure directing agents. A plausible mechanism of ZnO ND formation is proposed based on the control reaction conditions by varying the additive sequences of EC and CTAB and previous works available in literature. In the presence of only EC, ZnO NSs are obtained, while, in the presence of only CTAB, ZnO NRs formation is observed due to CTAB assisted *c*-axis growth of ZnO crystal. Photovoltaic properties of the hexagon shaped ZnO NDs as a photoanodic material for CdS/CdSe co-sensitized solar cells shows a PCE up to ∼4.86%. The superiority of the ZnO ND based device is proved by comparing the cell performance with the similar device fabricated with conventional ZnO NPs (PCE ∼ 3.14%), ZnO NRs (PCE ∼ 2.52%), and ZnO NSs (PCE ∼ 1.64%). Higher PCE obtained for the ZnO ND based device is mainly due to efficient photoinduced charge separation boosted by the exposed polar ±(0001) facets. EIS analysis further explains higher V_{oc} and FF values for the ZnO ND based photoanode attributed to slower electron−hole (e^-−h^+) recombination rate and faster charge migration. A larger value of photoinduced electron lifetime is observed in the case of ZnO ND photovoltaic device relative to all other fabricated devices which confirms minimum leakage of trapped electrons in the conduction band level of ZnO NDs, resulting in higher values of V_{oc} and J_{sc}.

ASSOCIATED CONTENT

Ⓢ Supporting Information

Table S1 listing the present scenario of ZnO based CdS/CdSe co-sensitized solar cells and their relevant performance parameters along with our results, calculated crystallite sizes of the synthesized particles, and ratios of I_b to I_d, figures showing schematic presentation of CdS and CdSe sensitization of the ZnO photoanodes, digital photographs of 1 wt % EC solution in only 1-butanol and in 1-butanol:water (3:1) solvent systems, photoluminescence spectra of ZnO NDs and ZnO NRs before and after calcination, powder X-ray diffraction patterns for the photoanodes (a) ZnO ND-CdS-CdSe2.0 and (b) ZnO ND-CdS-CdSe1.5, UV−vis diffuse reflectance spectra of CdS/CdSe co-sensitized ZnO ND, ZnO NP, ZnO NR, and ZnO NS based photoanodes with 1.5 mM Se precursor concentration, FESEM images of ZnO NSs, FESEM images of ZnO NDs' thickness and longitudinal dimension, and a size distribution plot for ZnO NDs in ethanol obtained from DLS, text describing crystallite size calculation for the synthesized materials and estimation of average particle size, and schematic presentation showing charge recombination in ZnO ND-CdS-CdSe(2.0mM) photoanode compared to the ZnO ND-CdS-CdSe(1.5mM). The Supporting Information is available free of charge on the ACS Publications website at DOI: 10.1021/acsami.5b01039.

AUTHOR INFORMATION

Corresponding Author

*Tel.: +91-361-2582320. Fax: +91-3612582349. E-mail: mq@iitg.ernet.in.

Notes

The authors declare no competing financial interest.

ACKNOWLEDGMENTS

We acknowledge the Council of Scientific and Industrial Research, India, for financial support through Project No. CSIR/01(2704)/12/EMR-II. The infrastructure and instrumentation help from IIT Guwahati and CIF, IIT Guwahati are acknowledged.

REFERENCES

(1) Anta, J. A.; Guillen, E.; Tena-Zaera, R. ZnO-Based Dye-Sensitized Solar Cells. *J. Phys. Chem. C* **2012**, *116*, 11413−11425.

(2) Xu, F.; Sun, L. Solution-Derived ZnO Nanostructures for Photoanodes of Dye-Sensitized Solar Cells. *Energy Environ. Sci.* **2011**, *4*, 818−841.

(3) Guillen, E.; Peter, L. M.; Anta, J. A. Electron Transport and Recombination in ZnO-Based Dye Sensitized Solar Cells. *J. Phys. Chem. C* **2011**, *115*, 22622−22632.

(4) Ramgir, N. S.; Mulla, I. S.; Pillai, V. K. Micropencils and Microhexagonal Cones of ZnO. *J. Phys. Chem. B* **2006**, *110*, 3995−4001.

(5) Ramgir, N. S.; Late, D. J.; Bhise, A. B.; More, M. A.; Mulla, I. S.; Joag, D. S.; Vijayamohanan, K. ZnO Multipods, Submicron Wires, and Spherical Structures and Their Unique Field Emission Behavior. *J. Phys. Chem. B* **2006**, *110*, 18236−18242.

(6) Chetia, T. R.; Barpuzary, D.; Qureshi, M. Enhanced Photovoltaic Performance Utilizing Effective Charge Transfer and Light Scattering Effects by the Combination of Mesoporous, Hollow 3D-ZnO along with 1D-ZnO in CdS Quantum Dot Sensitized Solar Cells. *Phys. Chem. Chem. Phys.* **2014**, *16*, 9625−9633.

(7) Liu, L.; Fu, L.; Liu, Y.; Liu, Y.; Jiang, P.; Liu, S.; Gao, M.; Tang, Z. Bioinspired Synthesis of Vertically Aligned ZnO Nanorod Arrays: Toward Greener Chemistry. *Cryst. Growth Des.* **2009**, *9*, 4793−4796.

(8) Law, M.; Greene, L. E.; Johnson, J. C.; Saykally, R.; Yang, P. Nanowire Dye-Sensitized Solar Cells. *Nat. Mater.* **2005**, *4*, 455−459.

(9) Li, C.; Yang, L.; Xiao, J.; Wu, Y.-C.; Søndergaard, M.; Luo, Y.; Li, D.; Meng, Q.; Iversen, B. B. ZnO Nanoparticle Based Highly Efficient CdS/CdSe Quantum Dot-Sensitized Solar Cells. *Phys. Chem. Chem. Phys.* **2013**, *15*, 8710−8715.

(10) Barceló, I.; Lana-Villarreal, T.; Gómez, R. Efficient Sensitization of ZnO Nanoporous Films with CdSe QDs Grown by Successive Ionic Layer Adsorption and Reaction (SILAR). *J. Photochem. Photobiol., A* **2011**, *220*, 47−53.

(11) Seol, M.; Kim, H.; Taka, Y.; Yong, K. Novel Nanowire Array Based Highly Efficient Quantum Dot Sensitized Solar Cell. *Chem. Commun. (Cambridge, U. K.)* **2010**, *46*, 5521−5523.

(12) Seol, M.; Ramasamy, E.; Lee, J.; Yong, K. Highly Efficient and Durable Quantum Dot Sensitized ZnO Nanowire Solar Cell Using Noble-Metal-Free Counter Electrode. *J. Phys. Chem. C* **2011**, *115*, 22018−22024.

(13) Chen, J.; Wu, J.; Lei, W.; Song, J. L.; Deng, W. Q.; Sun, X. W. Co-Sensitized Quantum Dot Solar Cell Based On ZnO Nanowire. *Appl. Surf. Sci.* **2010**, *256*, 7438−7441.

(14) Barpuzary, D.; Patra, A. S.; Vaghasiya, J. V.; Solanki, B. G.; Soni, S. S.; Qureshi, M. Highly Efficient One-Dimensional ZnO Nanowire-Based Dye-Sensitized Solar Cell Using a Metal-Free, D−π−A-Type, Carbazole Derivative with More than 5% Power Conversion. *ACS Appl. Mater. Interfaces* **2014**, *6*, 12629−12639.

(15) Luo, L.; Lv, G.; Li, B.; Hu, X.; Jin, L.; Wang, J.; Tang, Y. Formation of Aligned ZnO Nanotube Arrays by Chemical Etching and Coupling with CdSe For Photovoltaic Application. *Thin Solid Films* **2010**, *518*, 5146−5152.

(16) Cheng, H. M.; Huang, K. Y.; Lee, K. M.; Yu, P.; Lin, S. C.; Huang, J. H.; Wu, C. G.; Tang, J. High-Efficiency Cascade CdS/CdSe Quantum Dot-Sensitized Solar Cells Based on Hierarchical Tetrapod-Like ZnO Nanoparticles. *Phys. Chem. Chem. Phys.* **2012**, *14*, 13539−13548.

(17) Lin, C. Y.; Lai, Y. H.; Chen, H. W.; Chen, J. G.; Kung, C. W.; Vittal, R.; Ho, K. C. Highly Efficient Dye-Sensitized Solar Cell with a ZnO Nanosheet-Based Photoanode. *Energy Environ. Sci.* **2011**, *4*, 3448−3455.

(18) Jiang, C. Y.; Sun, X. W.; Lo, G. Q.; Kwong, D. L. Improved Dye-Sensitized Solar Cells with a ZnO-Nanoflower Photoanode. *Appl. Phys. Lett.* **2007**, *90*, 263501−263503.

(19) Tian, J.; Lv, L.; Wang, X.; Fei, C.; Liu, X.; Zhao, Z.; Wang, Y.; Cao, G. Microsphere Light-Scattering Layer Assembled by ZnO Nanosheets for the Construction of High Efficiency (>5%) Quantum Dots Sensitized Solar Cells. *J. Phys. Chem. C* **2014**, *118*, 16611−16617.

(20) Dong, Z.; Lai, X.; Halpert, J. E.; Yang, N.; Yi, L.; Zhai, J.; Wang, D.; Tang, Z.; Jiang, L. Accurate Control of Multishelled ZnO Hollow Microspheres for Dye-Sensitized Solar Cells with High Efficiency. *Adv. Mater.* **2012**, *24*, 1046−1049.

(21) Navaneethan, M.; Archana, J.; Arivanandhan, M.; Hayakawa, Y. Chemical Synthesis of ZnO Hexagonal Thin Nanodisks and Dye-Sensitized Solar Cell Performance. *Phys. Status Solidi RRL* **2012**, *6*, 120−122.

(22) Wang, J. X.; Wu, C. M. L.; Cheung, W. S.; Luo, L. B.; He, Z. B.; Yuan, G. D.; Zhang, W. J.; Lee, C. S.; Lee, S. T. Synthesis of Hierarchical Porous ZnO Disklike Nanostructures for Improved Photovoltaic Properties of Dye-Sensitized Solar Cells. *J. Phys. Chem. C* **2010**, *114*, 13157−13161.

(23) Boppella, R.; Anjaneyulu, K.; Basak, P.; Manorama, S. V. Facile Synthesis of Face Oriented ZnO Crystals: Tunable Polar Facets and Shape Induced Enhanced Photocatalytic Performance. *J. Phys. Chem. C* **2013**, *117*, 4597−4605.

(24) Jang, E. S.; Won, J. H.; Hwang, S. J.; Choy, J. H. Fine Tuning of the Face Orientation of ZnO Crystals to Optimize Their Photocatalytic Activity. *Adv. Mater.* **2006**, *18*, 3309−3312.

(25) Xu, L.; Hu, Y. L.; Pelligra, C.; Chen, C. H.; Jin, L.; Huang, H.; Sithambaram, S. K.; Aindow, M.; Joesten, R.; Suib, S. L. ZnO with Different Morphologies Synthesized by Solvothermal Methods for Enhanced Photocatalytic Activity. *Chem. Mater.* **2009**, *21*, 2875−2885.

(26) Huang, M.; Weng, S.; Wang, B.; Hu, J.; Fu, X.; Liu, P. Various Facets Tunable ZnO Crystals by a Scalable Solvothermal Synthesis and Their Facet-Dependent Photocatalytic Activities. *J. Phys. Chem. C* **2014**, *118*, 25434−25440.

(27) Huang, M.; Yan, Y.; Feng, W.; Weng, S.; Zheng, Z.; Fu, X.; Liu, P. Controllable Tuning Various Ratios of ZnO Polar Facets by Crystal Seed-Assisted Growth and Their Photocatalytic Activity. *Cryst. Growth Des.* **2014**, *14*, 2179−2186.

(28) Han, X. G.; He, H. Z.; Kuang, Q.; Zhou, X.; Zhang, X. H.; Xu, T.; Xie, Z. X.; Zheng, L. S. Controlling Morphologies and Tuning the Related Properties of Nano/Microstructured ZnO Crystallites. *J. Phys. Chem. C* **2009**, *113*, 584−589.

(29) Mclaren, A.; Valdes-Solis, T.; Li, G.; Tsang, S. C. Shape and Size Effects of ZnO Nanocrystals on Photocatalytic Activity. *J. Am. Chem. Soc.* **2009**, *131*, 12540−12541.

(30) Meagley, K. L.; Garcia, S. P. Chemical Control of Crystal Growth with Multidentate Carboxylate Ligands: Effect of Ligand Denticity on Zinc Oxide Crystal Shape. *Cryst. Growth Des.* **2011**, *12*, 707−713.

(31) Li, F.; Ding, Y.; Gao, P.; Xin, X.; Wang, L. Z. Single-Crystal Hexagonal Disks and Rings of ZnO: Low-Temperature, Large-Scale Synthesis and Growth Mechanism. *Angew. Chem.* **2004**, *116*, 5350−5354.

(32) Changb, P. R.; Yua, J.; Ma, X. Preparation of Porous Starch and Its Use as a Structure-Directing Agent for Production of Porous Zinc Oxide. *Carbohydr. Polym.* **2011**, *83*, 1016−1019.

(33) Kavitha, M. K.; John, H.; Gopinath, P. Polyvinyl Pyrrolidone Assisted Low Temperature Synthesis of ZnO Nanocones and Its Linear and Nonlinear Optical Studies. *Mater. Res. Bull.* **2014**, *49*, 132−137.

(34) Rao, J.; Yu, A.; Shao, C.; Zhou, X. Construction of Hollow and Mesoporous ZnO Microsphere: A Facile Synthesis and Sensing Property. *ACS Appl. Mater. Interfaces* **2012**, *4*, 5346−5352.

(35) Wang, A. J.; Liao, Q. C.; Feng, J. J.; Zhang, P. P.; Li, A. Q.; Wang, J. J. Apple Pectin-Mediated Green Synthesis Of Hollow Double-Caged Peanut-Like ZnO Hierarchical Superstructures and Photocatalytic Applications. *CrystEngComm* **2012**, *14*, 256−263.

(36) Tseng, Y. H.; Lin, H. Y.; Liu, M. H.; Chen, Y. F.; Mou, C. Y. Biomimetic Synthesis of Nacrelike Faceted Mesocrystals of ZnO-Gelatin Composite. *J. Phys. Chem. C* **2009**, *113*, 18053−18061.

(37) Ma, J.; Su, S.; Fu, W.; Yang, H.; Zhou, X.; Yao, H.; Chen, Y.; Yang, L.; Sun, M.; Mu, Y.; Lv, P. Synthesis of ZnO Nanosheet Array Film with Dominant {0001} Facets and Enhanced Photoelectrochemical Performance Co-sensitized by CdS/CdSe. *CrystEngComm* **2014**, *16*, 2910−2916.

(38) Chen, H.; Li, W.; Liu, H.; Zhu, L. CdS Quantum Dots Sensitized Single- and Multi-layer Porous ZnO Nanosheets for Quantum Dots-Sensitized Solar Cells. *Electrochem. Commun.* **2011**, *13*, 331−334.

(39) Yu, W. W.; Qu, L.; Guo, W.; Peng, X. Experimental Determination of the Extinction Coefficient of CdTe, CdSe, and CdS Nanocrystals. *Chem. Mater.* **2003**, *15*, 2854−2860.

(40) Leatherdale, C. A.; Woo, W. K.; Mikulec, F. V.; Bawendi, M. G. On the Absorption Cross Section of CdSe Nanocrystal Quantum Dots. *J. Phys. Chem. B* **2002**, *106*, 7619−7622.

(41) Kan, S.; Mokari, T.; Rothenberg, E.; Banin, U. Synthesis and Size-Dependent Properties of Zinc-Blende Semiconductor Quantum Rods. *Nat. Mater.* **2003**, *2*, 155−158.

(42) Trinh, M. T.; Houtepen, A. J.; Schins, J. M.; Hanrath, T.; Piris, J.; Knulst, W.; Goossens, A. P. L. M.; Siebbeles, L. D. A. In Spite of Recent Doubts Carrier Multiplication Does Occur in PbSe Nanocrystals. *Nano Lett.* **2008**, *8*, 1713−1718.

(43) Kamat, P. V. Quantum Dot Solar Cells. The Next Big Thing in Photovoltaics. *J. Phys. Chem. Lett.* **2013**, *4*, 908−918.

(44) Mora-Sero, I.; Bisquert, J. J. Breakthroughs in the Development of Semiconductor-Sensitized Solar Cells. *J. Phys. Chem. Lett.* **2010**, *1*, 3046−3052.

(45) Li, L.; Yang, X.; Gao, J.; Tian, H.; Zhao, J.; Hagfeldt, A.; Sun, L. Highly Efficient CdS Quantum Dot-Sensitized Solar Cells Based on a Modified Polysulfide Electrolyte. *J. Am. Chem. Soc.* **2011**, *133*, 8458−8460.

(46) Ma, X.; Zhao, K.; Tang, H.; Chen, Y.; Lu, C.; Liu, W.; Gao, Y.; Zhao, H.; Tang, Z. New Insight into the Role of Gold Nanoparticles in Au@CdS Core−Shell Nanostructures for Hydrogen Evolution. *Small* **2014**, *10*, 4664−4670.

(47) Robel, I.; Subramanian, V.; Kuno, M.; Kamat, P. V. Quantum Dot Solar Cells. Harvesting Light Energy with CdSe Nanocrystals Molecularly Linked to Mesoscopic TiO_2 Films. *J. Am. Chem. Soc.* **2006**, *128*, 2385−2393.

(48) Plass, R.; Pelet, S.; Krueger, J.; Gratzel, M.; Bach, U. Quantum Dot Sensitization of Organic-Inorganic Hybrid Solar Cells. *J. Phys. Chem. B* **2002**, *106*, 7578−7580.

(49) Chang, J. Y.; Lin, J. M.; Su, L. F.; Chang, C. F. Improved Performance of $CuInS_2$ Quantum Dot-Sensitized Solar Cells Based on a Multilayered Architecture. *ACS Appl. Mater. Interfaces* **2013**, *5*, 8740−8752.

(50) Choi, Y. C.; Lee, D. U.; Noh, J. H.; Kim, E. K.; Seok, S. I. Highly Improved Sb_2S_3 Sensitized-Inorganic−Organic Heterojunction Solar Cells and Quantification of Traps by Deep-Level Transient Spectroscopy. *Adv. Funct. Mater.* **2014**, *24*, 3587−3592.

(51) Yin, X.; Battaglia, C.; Lin, Y.; Chen, K.; Hettick, M.; Zheng, M.; Chen, C. Y.; Kiriya, D.; Javey, A. 19.2% Efficient InP Heterojunction Solar Cell with Electron-Selective TiO_2 Contact. *ACS Photonics* **2014**, *1*, 1245−1250.

(52) Zhu, G.; Pan, L.; Xu, T.; Sun, Z. CdS/CdSe-Cosensitized TiO_2 Photoanode for Quantum-Dot-Sensitized Solar Cells by a Microwave Assisted Chemical Bath Deposition Method. *ACS Appl. Mater. Interfaces* **2011**, 3, 3146−3151.

(53) Santra, P. K.; Kamat, P. V. Mn-Doped Quantum Dot Sensitized Solar Cells: A Strategy to Boost Efficiency Over 5%. *J. Am. Chem. Soc.* **2012**, *134*, 2508−2511.

(54) Chong, L. W.; Chien, H. T.; Lee, Y. L. Assembly of CdSe onto Mesoporous TiO_2 Films Induced by a Self-Assembled Monolayer for Quantum Dot-Sensitized Solar Cell Applications. *J. Power Sources* **2010**, *195*, 5109−5113.

(55) Tian, J.; Uchaker, E.; Zhang, Q.; Cao, G. Hierarchically Structured ZnO Nanorods−Nanosheets for Improved Quantum-Dot-Sensitized Solar Cells. *ACS Appl. Mater. Interfaces* **2014**, *6*, 4466−4472.

(56) Barpuzary, D.; Khan, Z.; Vinothkumar, N.; De, M.; Qureshi, M. Hierarchically Grown Urchinlike CdS@ZnO and CdS@Al_2O_3 Heteroarrays for Efficient Visible-Light-Driven Photocatalytic Hydrogen Generation. *J. Phys. Chem. C* **2012**, *116*, 150−156.

(57) Xu, C. X.; Sun, X. W.; Dong, Z. L.; Yu, M. B. Zinc Oxide Nanodisk. *Appl. Phys. Lett.* **2004**, *85*, 3878−3880.

(58) Jin, H.; Zhou, W.; Cao, J.; Stoyanov, D. S.; Blijdenstein, T. B. J.; de Groot, P. W. N.; Arnaudov, L. N.; Pelan, E. G. Super Stable Foams Stabilized by Colloidal Ethyl Cellulose Particles. *Soft Matter* **2012**, *8*, 2194−2205.

(59) Sun, X. M.; Chen, X.; Deng, Z. X.; Li, Y. D. A CTAB-Assisted Hydrothermal Orientation Growth of ZnO Nanorods. *Mater. Chem. Phys.* **2002**, *78*, 99−104.

(60) Wu, X. L.; Siu, G. G.; Fu, C. L.; Ong, H. C. Photoluminescence and Cathodoluminescence Studies of Stoichiometric and Oxygen Deficient ZnO Films. *Appl. Phys. Lett.* **2001**, *78*, 2285−2287.

(61) Zeng, H.; Duan, G.; Li, Y.; Yang, S.; Xu, X.; Cai, W. Blue Luminescence of ZnO Nanoparticles Based on Non-Equilibrium Processes: Defect Origins and Emission Controls. *Adv. Funct. Mater.* **2010**, *20*, 561−572.

(62) Choi, Y.; Seol, M.; Kim, W.; Yong, K. Chemical Bath Deposition of Stoichiometric CdSe Quantum Dots for Efficient Quantum-Dot-Sensitized Solar Cell Application. *J. Phys. Chem. C* **2014**, *118*, 5664−5670.

(63) Qureshi, M.; Chetia, T. R.; Ansari, M. S.; Soni, S. S. Enhanced Photovoltaic Performance of Meso-porous SnO_2 Based Solar Cells Utilizing 2D MgO Nanosheets Sensitized by a Metal Free Carbazole Derivative. *J. Mater. Chem. A* **2015**, 3, 4291−4300.

(64) Barpuzary, D.; Qureshi, M. Enhanced Photovoltaic Performance of Semiconductor-Sensitized ZnO−CdS Coupled with Graphene Oxide as a Novel Photoactive Material. *ACS Appl. Mater. Interfaces* **2013**, *5*, 11673−11682.

(65) Chen, Y.; Zhang, L.; Ning, L.; Zhang, C.; Zhao, H.; Liu, B.; Yang, H. Superior Photocatalytic Activity of Porous Wurtzite ZnO Nanosheets with Exposed {001} Facets and a Charge Separation Model Between Polar (001) and ($00\bar{1}$) Surfaces. *Chem. Eng. J.* **2015**, *264*, 557−564.

(66) Phadke, S.; Pasquier, A. D.; Birnie, D. P. Enhanced Electron Transport through Template-Derived Pore Channels in Dye-Sensitized Solar Cells. *J. Phys. Chem. C* **2011**, *115*, 18342−18347.

(67) Kern, R.; Sastrawan, R.; Ferber, J.; Stangl, R.; Luther, J. Modeling and Interpretation of Electrical Impedance Spectra of Dye Solar Cells Operated under Open-Circuit Conditions. *J. Electrochim. Acta* **2002**, *47*, 4213−4225.